# Design and Optimization of Reverse Salient Permanent Magnet Synchronous Motor Based on Controllable Leakage Flux

Longxin Du, Xiping Liu, Jiesheng Fu, Jianwei Liang, and Chaozhi Huang

***Abstract*—In this paper, a controllable leakage flux reverse salient permanent magnet synchronous motor(CLF-RSPMSM) is designed, which has the advantages of wide speed range and low irreversible demagnetization risk. Firstly, the principle of controllable leakage flux and reverse saliency effect is introduced, and the design of the rotor flux barrier is emphatically discussed. Secondly, multiple design variables are stratified by the comprehensive sensitivity method, and the main variables are screened out. Then the relationship between the main variables and the optimization goal is discussed according to the response surface diagram. Thirdly, a sequential nonlinear programming algorithm(SNP) is used to optimize the three optimization objectives comprehensively. Finally, the electromagnetic performance of the proposed motor is compared with the initial IPM motor, the mechanical strength of the proposed rotor is analyzed, and the results verify the effectiveness of the design and optimization method of the proposed motor.**

***Index Terms*—Controllable leakage flux, reverse saliency, comprehensive sensitivity, multi-objective optimization, wide speed range.**

## I. INTRODUCTION

IN recent years, permanent magnet synchronous motor (PMSM) has been widely studied and applied in the field of electric vehicles due to its advantages of high power/torque density and simple structure[1]-[3]. However, due to the constant permanent magnetic potential of this kind of motor, it is difficult to adjust the air gap flux, so the speed range of the flux-weakening field is narrow, and the efficiency is low when running at high speed, which cannot meet the comprehensive driving demand of the new generation of electric vehicles. Therefore, a reverse salient permanent magnet synchronous motor (RSPMSM) emerges at the right moment[4],[5]. It not only inherits the advantages of traditional motors, but also has the larger value of *d*-axis inductance $L_d$ to obtain a wide constant power speed range. Meanwhile, a positive *d*-axis current can be used to generate the effect of magnetic field enhancement, which can reduce the irreversible demagnetization risk of permanent magnets (PMs).

Generally speaking, to obtain a wide range of constant power and speed for the motor, it is mainly through the motor air-gap flux's effective adjustment. For the research of the vehicle-driven permanent magnet motor, the magnetic field of the hybrid excitation motor can be adjusted online by adding additional electric excitation winding[6], or by adding a negative *d*-axis flux-weakening current to weaken the magnetic field of the permanent magnet motor[7]. In [8] and [9], the internal magnetic field of the motor is adjusted by an external mechanical device. All these methods change the total flux of the excitation source to realize the regulation control of the effective main flux. The total flux includes the main flux and leakage flux. When the total flux of the excitation source remains unchanged, the leakage flux can be adjusted effectively theoretically by changing the leakage flux[10]-[12].

In this paper, a controllable leakage flux reverse salient permanent magnet synchronous motor (CLF-RSPMSM) is designed by combining the characteristics of controllable leakage flux and reverse saliency. By setting a magnetic bridge on the *d*-axis to increase the *d*-axis inductance $L_d$, adding a flux barrier on the *q*-axis and designing the leakage flux bypass, not only can the *q*-axis inductance $L_q$ be reduced and the reverse saliency characteristic be realized, but also the stator armature winding *d*-axis and *q*-axis magnetic circuit can be coupled with the permanent magnet leakage flux circuit. Then the motor speed range is effectively widened, and the low efficiency in the high-speed area is solved. At the same time, multi-objective optimization of the motor is carried out to meet the design requirements[13]-[16]. And compared with the traditional motor performance, further verify the effectiveness of the proposed motor.

## II. DESIGN PRINCIPLES AND MOTOR TOPOLOGY

### A. Reverse Saliency Characteristics

The most significant difference between the CLF-RSPMSM and the traditional IPM motor is the inductance characteristic. The inductance characteristic of the traditional IPM motor is $L_d<L_q$. In contrast, the inductance characteristic of the CLF-RSPMSM is $L_d>L_q$. At low speed, a positive reluctance torque can be obtained; at high speed, only a small *d*-axis flux-weakening current is needed to improve the range of flux-weakening field and reduce the irreversible demagnetization risk of the PM.

Manuscript received March 06, 2021; revised April 14, 2021; accepted June 03, 2021. date of publication June 25, 2021; date of current version June 18, 2021.

This work was supported by the National Natural Science Foundation of China under Grant no. 52067008, in part by the Plan Project of Jiangxi Province of P.R. China under grant no. GJJ160598 and 20181BAB206035, and in part by the Program of Qingjiang Excellent Young Talents. *(Corresponding Author:Longxin Du)*

Longxin Du, Xiping Liu, Jiesheng Fu, Jianwei Liang and Chaozhi Huang are with the Jiangxi University of Science and Technology, Ganzhou 341000, China (e-mail: 1439887078@qq.com).

Digital Object Identifier 10.30941/CESTEMS.2021.00020

The influence of reverse saliency characteristics on the working point of the PMs is also different from that of the traditional IPM motors. Fig.1 shows the voltage and current constraint circles of the two motors, respectively. As shown in Fig.1(a), for the traditional IPM motor with $L_d<L_q$, the maximum torque operating point is located in the second quadrant, and the maximum torque per ampere (MTPA) control method is adopted. The motor is always operating in a negative area of the *d*-axis current, flux-weakening state, which reduces the working point of the PMs. For the proposed motor with $L_d>L_q$, the maximum torque operating point is located in the first quadrant under MTPA control. Therefore, a positive *d*-axis current can improve the working point of the PMs, which is similar to the effect of magnetic field enhancement. As shown in Fig.1(b), the PMs working point moves from $H_0$ to $H_i$. Compared with the PMs working point $H_w$ of the traditional IPM motor, it is further away from the irreversible demagnetization point $H_k$.

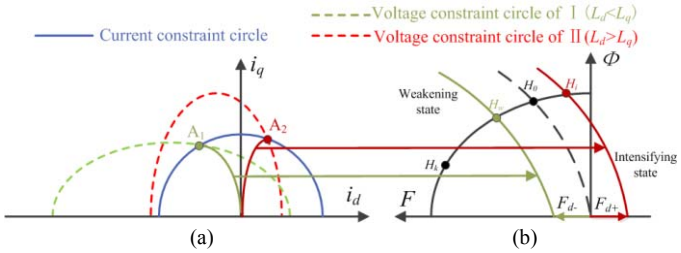


Fig.1. The relationships between different inductance characteristics and PMs operation points (a) Current-voltage constrain circles. (b) PMs operating points at different operation states.

## B. Principle of Controllable Leakage Flux

At the beginning of the design of the traditional permanent magnet motor, the main goal is to reduce leakage flux and make full use of permanent magnetic potential. Under the condition of ensuring the mechanical strength of the rotor, air barriers close to the air gap are usually set at both ends of the PMs to reduce the width of the magnetic bridge at the end. In this way, the utilization ratio of the PMs can be improved to some extent. However, in the flux-weakening process, the narrow bridge at the end of the magnetic barrier is easy to saturate, so that the magnetic flux loop of the *d*-axis armature demagnetization magnetic potential forms a barrier, and a large amount of demagnetization magnetic flux cannot pass through, causing difficulties for the flux-weakening lift rate.

Different from the traditional motor, a leakage flux controllable reverse salient pole motor is provided with a leakage flux bypass between the poles. When the motor is in a no-load state, the armature magnetic flux is zero, and a large number of a permanent magnetic flux forms leakage flux between adjacent poles through inter-pole leakage bypass. When the motor is transformed from no-load to heavy-load, the increase of *q*-axis current makes the inter-pole leakage flux bypass gradually saturated, so the permanent magnet leakage flux reduces, thus providing enough output torque. When the motor enters the state of flux-weakening, the *q*-axis current decreases, the saturation degree of inter-pole leakage flux bypass decreases, a large number of leakage flux exist in PMs, and the PMs flux chain of the motor decreases. In addition, the motor has a larger value of $L_d$, so only a small flux-weakening current is needed to widen the speed range, and the irreversible demagnetization risk of the PMs is reduced.

## C. Motor Topology Design

As shown in Fig.2, arc-shaped and elliptic magnetic barriers are set on the *q*-axis magnetic circuit of the rotor. Two leakage flux paths are constructed between the elliptic and arc-shaped magnetic barriers and the air gap, respectively. The distance between the arc-shaped magnetic barrier and the PMs is very small in order to reduce the self-leakage flux of the PMs. In addition, the elliptic and arc barriers increase the *q*-axis resistance and reduce the *q*-axis inductance. The curved magnetic barrier near the inner side of the rotor is also to reduce the *q*-axis inductance. In addition, Multilayer reluctance is reasonably set on both sides of the *d*-axis, and the magnetic bridge is set in PMs. This makes the reluctance of the magnetic circuit of the *d*-axis decrease, but that of the *q*-axis increases, so that the proposed motor has the characteristics of $L_d>L_q$.

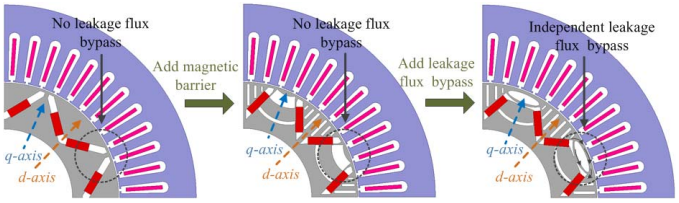


Fig.2. Rotor evolution. (a) Initial IPM motor ($L_d<L_q$). (b) RSPMSM ($L_d>L_q$). (c) Proposed CLF-RSPMSM ($L_d>L_q$).

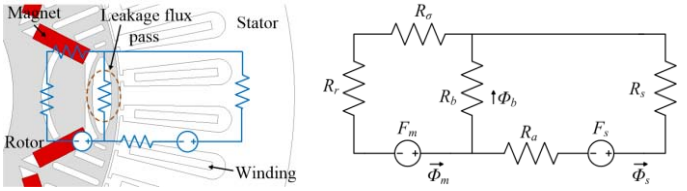


Fig.3. Explanation of the leakage flux pass of the CLF-RSPMSM. (a) Schematic drawing of the CLF-RSPMSM. (b) The magnetic circuit of the leakage flux pass.

Fig.3 shown the equivalent magnetic circuit diagram. The reluctance of air gap, leakage bypass, rotor and stator is $R_a$, $R_b$, $R_r$ and $R_s$, respectively. $R_\sigma$ represents the magnetic resistance of the PMs and partial magnetic barrier; The magnetomotive force of the PMs is set as $F_m$; The magnetomotive force generated by the stator armature reaction is set as $F_s$. The stator core flux and rotor core flux are $\Phi_s$ and $\Phi_m$, respectively. According to the characteristics of controllable leakage flux and the equivalent circuit, the leakage flux $\Phi_b$ is derived as follows:

$$\begin{bmatrix} \Phi_s \\ \Phi_m \end{bmatrix} = \frac{1}{\det G}\begin{bmatrix} R_r+R_b+R_\sigma & R_b \\ R_b & R_a+R_b+R_s \end{bmatrix}\begin{bmatrix} F_s \\ F_m \end{bmatrix} \quad (1)$$

$$\begin{aligned} \det G &= \begin{vmatrix} R_r+R_b+R_\sigma & R_b \\ R_b & R_a+R_b+R_s \end{vmatrix} \\ &= (R_r+R_b+R_\sigma)(R_a+R_b+R_s)-R_b^2 \end{aligned} \quad (2)$$

$$\begin{aligned} \Phi_b &= \Phi_m-\Phi_s \\ &= \frac{1}{\det G}\left[(R_a+R_s)F_m-(R_r+R_\sigma)F_s\right] \ge 0 \end{aligned} \quad (3)$$

$$\frac{F_s}{F_m} \le \frac{R_a + R_s}{R_r + R_\sigma} \tag{4}$$

In order to obtain controllable leakage flux characteristics, the leakage flux $\Phi_b$ needs to be greater than or equal to zero, as shown in (3). The conditions required to achieve the desired controllable leakage flux property are expressed as the relationship between $F_s$ and $F_m$, as shown by (4). The main design parameters of the CLF-RSPMSM are shown in Table Ⅰ.

TABLE Ⅰ
KEY DESIGN PARAMETERS OF CLF-RSPMSM

| Items | Initial IPM motor | CLF-RSPMSM |
|---|---|---|
| Rated out power | 10kW | |
| Slots/Poles | 48/8 | |
| Stator outer/inner diameter | 269.24/161.9mm | |
| Rotor outer/inner diameter | 160.4/100.64mm | |
| Rated phase current | 35A | |
| Rated speed | 1000rpm | |
| Turn numbers | 15 | |
| PM type | N38EH | |
| PM width/thickness | 16/5.6mm | 17.4/5.1mm |
| Air-gap length | 0.75mm | |

## III. MULTI-OBJECTIVE DESIGN OPTIMIZATION OF CLF-RSPMSM

Based on the above analysis, in order to achieve the best performance of all aspects of the proposed motor, multiple parameters need to be comprehensively optimized to obtain the optimal value. As shown in Fig.4, the optimization target is selected, and the sensitivity analysis method is adopted to analyze the sensitivity of multiple parameters and the optimization target. On the basis of the previous step, the parameters with high sensitivity are selected, and then the constraints of the optimization target are determined. The multi-objective optimization method based on the response surface is adopted to further optimize the proposed motor.

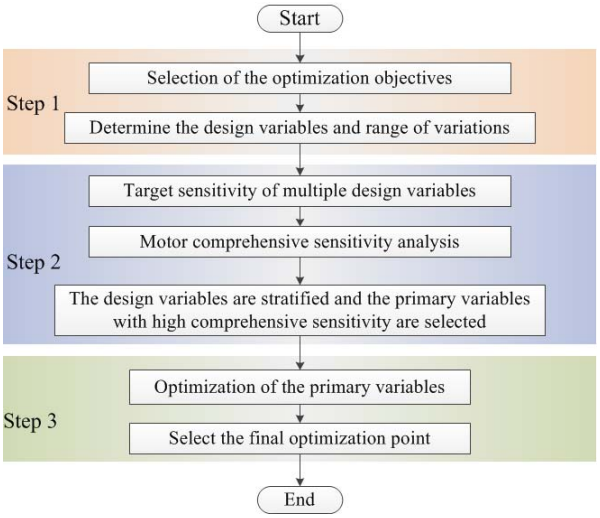


Fig.4. Optimization flowchart of the CLF-RSPMSM

### A. Optimization Objectives

The electromagnetic torque of the CLF-RSPMSM in the *d-q* synchronous reference frame is described as:

$$T_{em} = \frac{3}{2} p[\psi_{pm} i_q + (L_d - L_q) i_d i_q] \tag{5}$$

Where 3/2 $p\psi_{pm}$ $i_q$ is called permanent magnet torque and 3/2 $p(L_d\text{-}L_q)$ $i_d$ $i_q$ is called reluctance torque. $P$ is a number of pole-pair, $\psi_{pm}$ is the PM flux linkage, while $i_d$ and $i_q$ are the *d*-axis current and *q*-axis current.

Meanwhile, the torque ripple $T_{ripple\%}$ can be expressed as follows

$$T_{rippie\%} = \frac{T_{em\_max} - T_{em\_min}}{T_{em\_avg}} \times 100\% \tag{6}$$

Where $T_{em\_avg}$ is the average value of electromagnetic torque, $T_{em\_max}$ and $T_{em\_min}$ are the maximum and minimum values of electromagnetic torque.

In addition, compared with the initial motor, the salient feature of the CLF-RSPMSM is that the ratio of the *d*-axis inductance to the *q*-axis inductance is greater than one, which is defined as the reverse saliency ratio.

The value is defined as follows:

$$\varphi_{dq} = \frac{L_d}{L_q} \tag{7}$$

The greater the reverse saliency ratio, the greater the magnetic resistance torque will be under the positive *d*-axis current, and correspondingly, the electromagnetic torque will also be increased.

### B. Sensitivity Analysis

After the optimization goals are selected, the design variables of the proposed motor in this step and the corresponding variation range are shown in Table Ⅱ.

By means of sensitivity analysis, the more sensitive parameters can be selected, which have a more significant imp-

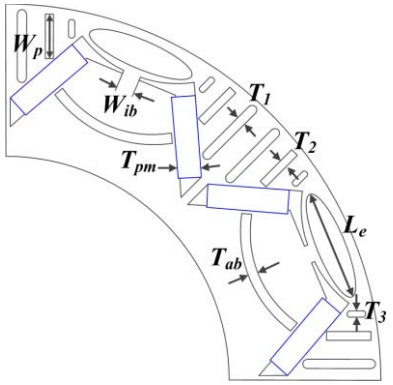


Fig.5. Parameterization of the proposed CLF-RSPMSM rotor structure.

TABLE Ⅱ
DESIGN VARIABLES AND VARIATION RANGES

| Design variables | Variation ranges |
|---|---|
| PMs thickness $T_{pm}$ | [4.8mm,5.2mm] |
| Medial arc barrier thickness $T_{ab}$ | [1.5mm,2.8mm] |
| 1st layer parallel barrier thickness $T_1$ | [1mm,2.4mm] |
| 2nd layer parallel barrier thickness $T_2$ | [1.5mm,2.1mm] |
| 3rd layer parallel barrier thickness $T_3$ | [1mm,2mm] |
| 2nd layer parallel barrier width $W_p$ | [8.5mm,10mm] |
| Inter-pole magnetic bridge width $W_{ib}$ | [2mm,5mm] |
| Long axis length of the elliptic magnetic barrier $L_e$ | [19mm,24mm] |

act on the motor optimization objectives, to improve the efficiency of traditional single-parameter optimization. The sensitivity index $S(xi)$ of the design variable to the optimization goal can be expressed as follows:

$$S(x_i)=\frac{V_{ar}(E(y/x_i))}{V_{ar}(y)} \tag{8}$$

Where $E(y/x_i)$ is the average value of the optimized target y when the design variable $x_i$ is unchanged, $V_{ar}$ $(E(y/x_i))$ is the variance of $E(y/x_i)$, and $V_{ar}$ $(y)$ is the variance of $y$. The higher the sensitivity index, the higher the influence of design variables on the optimization goal. If the sensitivity index is positive, there is a positive correlation between the optimization goal and the design variable. On the contrary, if the sensitivity index is negative, there is a negative correlation between the optimization goal and the design variable. Fig.6 shows the influence of each design variable on the optimization goals.

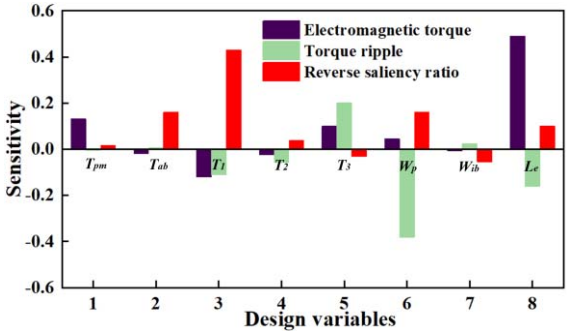


Fig.6. Sensitivity analysis of the design variables on the optimization goals.

As shown in Fig.6, For the electromagnetic torque, the design variable $L_e$ has a high sensitivity, which means that $L_e$ has a great influence on the electromagnetic torque.The sensitivity of $L_e$ is positive, so the electromagnetic torque increases with the increase of $L_e$. Similarly, the influence degree of other design variables on the optimization goal can be obtained.

However, this result can only analyze the sensitivity of a single variable to a single target, so this paper adopts a comprehensive sensitivity analysis method to accurately select the main design variables. The comprehensive sensitivity of the proposed motor is as follows:

$$S_{CLF\text{-}RSPMSM}(x_i)=\lambda_t\left|S_t(x_i)\right|+\lambda_{ri}\left|S_{ri}(x_i)\right|+\lambda_\varphi\left|S_\varphi(x_i)\right| \tag{9}$$

where $S_{CLF\text{-}RSPMSM}$ $(x_i)$ is the comprehensive sensitivity of the motor, while $x_i$ is the parameter variable to be optimized. $\lambda_t$, $\lambda_{ri}$, $\lambda_\varphi$ are the weight coefficient of electromagnetic torque, torque ripple and reverse saliency ratio respectively, and $\lambda_t+\lambda_{ri}+\lambda_\varphi=1$. $|S_t(x_i)|$, $|S_{ri}(x_i)|$ and $|S_\varphi(x_i)|$ are the absolute value of the sensitivity index of design variables to electromagnetic torque, torque ripple and reverse saliency ratio, respectively. The proposed motor is mainly aimed at the field of electric vehicles, which requires high torque output capacity of the proposed motor. Therefore, according to previous design experience, the $\lambda_t$ was set at 0.4 to improve its priority. $\lambda_{ri}$ and $\lambda_\varphi$ are set to 0.3. As shown in Table Ⅲ.

Eight design variables are selected for the proposed motor, and it takes time to optimize these variables simultaneously. According to the degree of comprehensive sensitivity index, the primary variables are selected to improve the optimization

TABLE Ⅲ
DESIGN VARIABLES AND SENSITIVITY INDEX

| Variables | Optimization goals | | | Comprehensive sensitivity index |
|---|---|---|---|---|
| | $S_t(x_i)$ $\lambda_t$=0.4 | $S_{ri}(x_i)$ $\lambda_{ri}$=0.3 | $S_\varphi(x_i)$ $\lambda_\varphi$=0.3 | |
| $T_{pm}$ | 0.13 | -0.0043 | 0.015 | 0.05779 |
| $T_{ab}$ | -0.017 | 0.0067 | 0.16 | 0.05681 |
| **$T_1$** | **-0.12** | **-0.11** | **0.43** | **0.21** |
| $T_2$ | -0.023 | -0.056 | 0.037 | 0.0371 |
| **$T_3$** | **0.1** | **0.2** | **-0.03** | **0.109** |
| **$W_p$** | **0.044** | **-0.38** | **0.16** | **0.1796** |
| $W_{ib}$ | -0.0059 | 0.023 | -0.054 | 0.02546 |
| **$L_e$** | **0.49** | **-0.16** | **0.099** | **0.2737** |

TABLE Ⅵ
DESIGN VARIABLE STRATIFICATION RESULT

| | | |
|---|---|---|
| CLF-RSPMSM | Primary variables | $T_1$、 $T_3$ 、$W_p$、 $L_e$ |
| | Non-primary variables | $T_{pm}$、 $T_{ab}$、 $T_2$ 、$W_{ib}$ |

efficiency of the proposed motor. The sensitivity accuracy determined in this paper is 0.1. When the comprehensive sensitivity is greater than or equal to 0.1, the design variable is set as the primary variable. When the comprehensive sensitivity is less than or equal to 0.1, the design variable is set as a non-primary variable. The stratification results of design variables are listed in Table Ⅵ.

For the primary variables, the response is adopted to optimize them to improve the accuracy and efficiency of the whole motor. For non-primary variable , the initial value can be set in the next stage of optimization due to its small influence.

### C. *Objective Optimization*

The weight coefficient is added to the optimization objective. The objective optimization function of the proposed motor can be expressed as:

$$F(x_i)_{min}=\lambda_t\frac{T'_{em}(x_i)}{T_{em}(x_i)}+\lambda_{ri}\frac{T'_{ripple\%}(x_i)}{T_{ripple\%}(x_i)}+\lambda_\varphi\frac{\varphi'_{dq}(x_i)}{\varphi_{dq}(x_i)} \tag{10}$$

Where, $\min x_i \le x_i \le \max x_i$, $i$=1, 2, 3, $T'_{em}(x_i)$, $T'_{ripple\%}(x_i)$, $\varphi'_{dq}(x_i)$ are the initial values of electromagnetic torque, torque ripple and reverse saliency ratio respectively. $T_{em}(x_i)$, $T_{ripple\%}(x_i)$, $\varphi_{dq}(x_i)$ are the optimal value of electromagnetic torque, torque ripple and reverse saliency ratio, respectively.

The constraint of the proposed motor optimization objective is

$$T_{em}\ge 80\text{Nm};\quad T_{ripple\%}\le 15\%;\quad \varphi_{dq}\ge 1.2 \tag{11}$$

In the optimization process of the main variables, in order to accurately obtain the influence relationship between the main variables and the optimization goal. The response surface analysis method can be used to know the impact of the main variables on each optimization goal has a certain conflict. Take the main variables $T_1$ and $T_3$ as examples, and draw the response surface diagram of them and the three optimization objectives. As is shown in Fig.7, with the increase of $T_1$, the electromagnetic torque first increases and then decreases, while the torque ripple first increases, then decreases and then increases again, while the reverse saliency ratio gradually

increases.With the increase of $T_3$, both the electromagnetic torque and the torque ripple increase gradually, while the reverse saliency ratio decreases. Thus, it is difficult to accurately determine the optimal design value of major variables through univariate analysis, and reasonable tradeoffs between the three optimization objectives need to be further made.

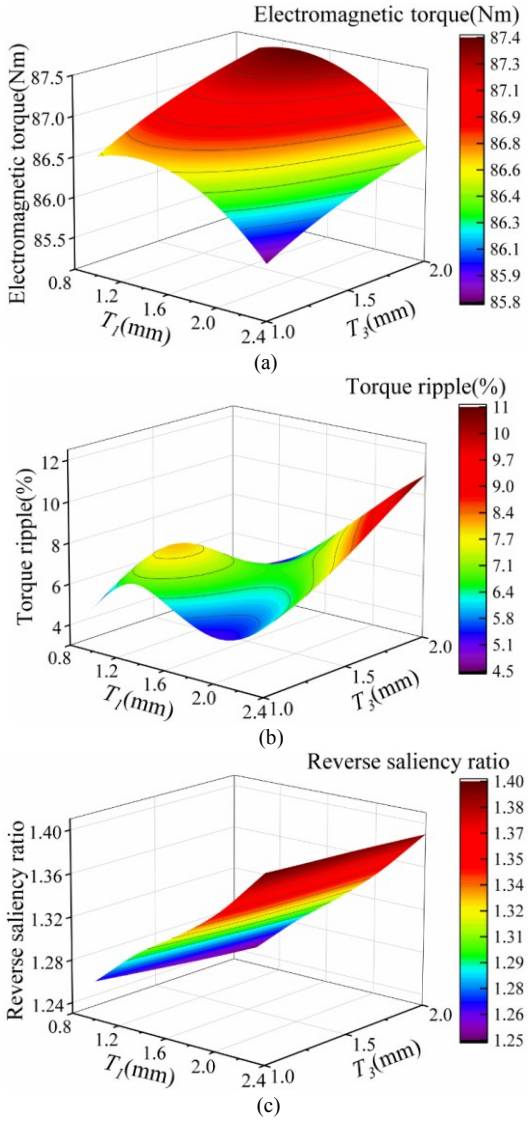


Fig.7. Response surface of $T_1$ and $T_3$ with three optimization goals. (a) Torque. (b) Torque ripple. (c) Reverse saliency ratio.

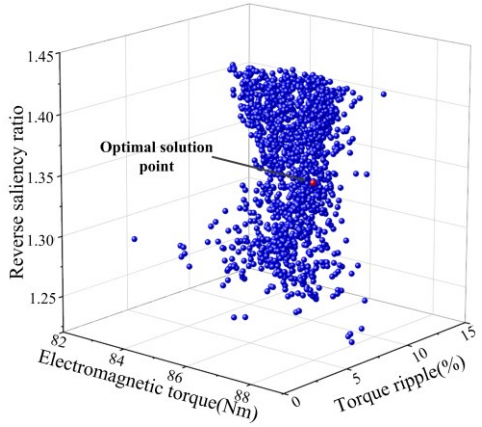


Fig.8. The relationship between the three optimization goals

In order to solve the tradeoff between multiple optimization objectives, a sequential nonlinear programming method (SNP) is also adopted in this part, which can be used to solve the comprehensive optimal solution of multiple optimization objectives. The solution of the formula can be obtained according to the SNP method theory and the above constraint conditions. Fig.8 shows the tradeoff between the three optimization objectives, and the red points are the optimal solution point. At the same time, the optimal value of the main variable of the proposed motor after optimization is given in TABLE Ⅴ.

TABLE Ⅴ
OPTIMIZATION RESULTS OF PRIMARY VARIABLES

| CLF-RSPMSM | | Initial values | Optimal values |
|---|---|---|---|
| Design variables | $T_1$ | 1mm | 2.09mm |
| | $T_3$ | 1.75mm | 2mm |
| | $L_e$ | 21mm | 23.63mm |
| | $W_p$ | 9mm | 9.5mm |
| optimization objectives | $T_{em}$ | 80.9Nm | 86.6Nm |
| | $T_{ripple\%}$ | 9.0% | 5.9% |
| | $\varphi_{dq}$ | 1.31 | 1.35 |

## IV. MOTOR COMPREHENSIVE PERFORMANCE COMPARISON AND ANALYSIS

### A. Performance of Controllable Leakage Flux

The CLF-RSPMSM studied in this paper can adjust the air-gap magnetic field of the motor by adjusting the $q$-axis current. In order to verify its controllable characteristics of leakage flux, Fig.9 shows the leakage flux distribution of $i_q$=0A, 50A, simulating the no-load and heavy-load conditions of the motor, respectively. It can be seen that in the no-load state, a large amount of magnetic flux flows to the adjacent pole through the leakage flux bypass, forming the inter-pole leakage flux. Under the heavy-load condition, the leakage flux between poles decreases obviously, and the flux flows to the stator through the bypass path.

In order to more intuitively display the magnetic regulation characteristics of the proposed motor, Fig.10 shows the curve of the $d$-axis flux linkage of the motor changing with the $q$-axis current. The $d$-axis current is set to zero, and only the $q$-axis current is added to avoid being affected by the stator reaction force. The minimum value of the motor is 0.2446 Wb when the motor is under no-load. With the continuous increase of the $q$-axis current, the $d$-axis flux linkage also increases, and the inter-pole leakage flux also decreases. When the current increases to the stator and rotor saturation, the flux linkage tends to be flat and reaches a maximum value of 0.2904Wb, and the flux change rate in this process is about 18.7%. The results effectively verify that the proposed motor has controllable leakage flux characteristics.

Since the $d$-axis flux linkage increases with the increase of the $q$-axis current, the torque changes with the current show new characteristics, and the relationship between them is no longer a linear one without leakage flux. According to the finite element simulation results in Fig.10(b), it can be seen that the torque of the proposed motor varies with the $q$-axis current,

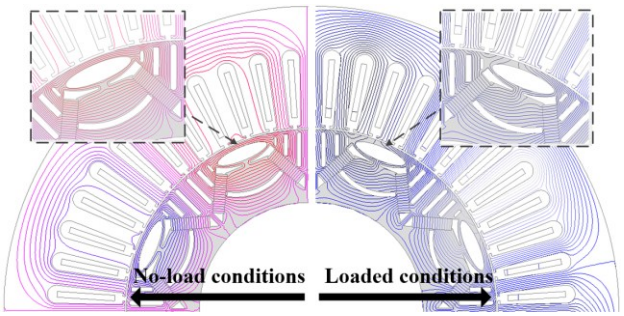


(a) (b)

Fig.9. Variable leakage flux characteristics of the CLF-RSPMSM. (a) No-load ($i_q$=0A). (b) Loaded condition ($i_q$=50A).

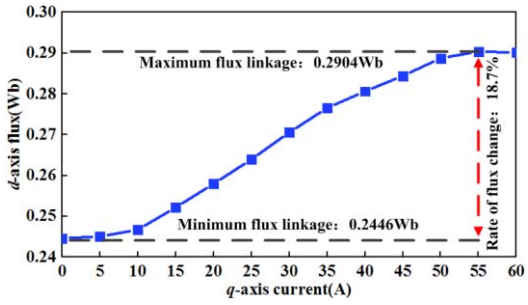


(a)

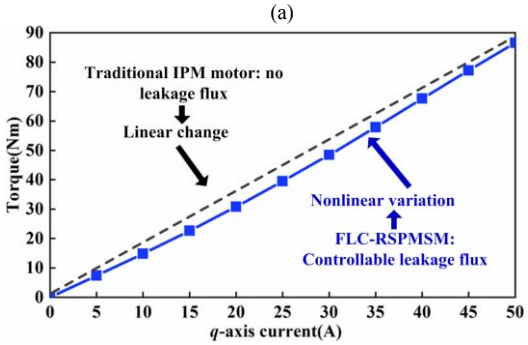


(b)

Fig.10. Controllable leakage flux characteristics of the CLF-RSPMSM. (a) *D*-axis flux linkage. (b) Torque.

which is a slightly concave curve.

### B. D-Axis and Q-Axis Inductances

In the following sections, in order to verify the rationality of the proposed motor design, the finite-element analysis method is used to analyze and compare the proposed motor with the initial IPM motor. The two motors have the same parameters except for the difference in rotor structure.

Compared with the initial IPM motor, the proposed motor has the controllable leakage flux characteristics, and the biggest difference is that the reverse saliency ratio of the motor is $\varphi_{dq}$>1. The reverse saliency ratio of the initial IPM motor is $\varphi_{dq}$<1. Fig.11 shows the reverse saliency ratio and inductance difference of the two motors as the current amplitude $I_{max}$ changes from 0A to 100A. As expected, in the process of the initial IPM motor from no-load to heavy-load, the reverse saliency ratio is always less than one, and the difference between $L_d$ and $L_q$ is negative. On the contrary, in this process, the reverse saliency ratio of the proposed motor is greater than one, and the difference between $L_d$ and $L_q$ is maintained at more than 2.5mH under heavy-load. This means that the proposed motor has a larger value of $L_d$, preliminarily verified that the

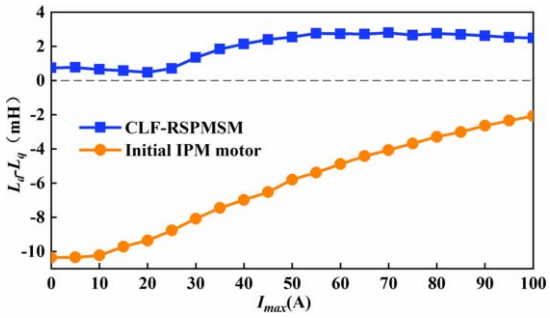


(a)

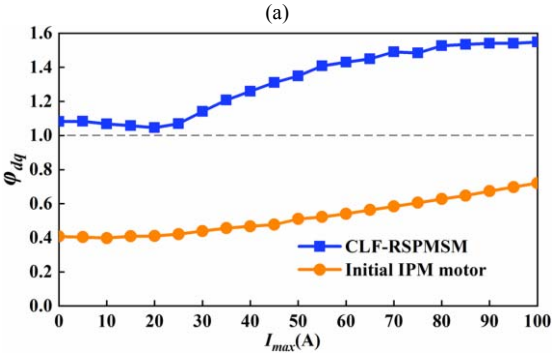


(b)

Fig.11. Inductance characteristics of the CLF-RSPMSM and initial IPM motor. (a) Inductance difference between *d*-axis and *q*-axis. (b) The reverse saliency ratio.

motor has a wide range of speed regulation.

### C. Torque Characteristics

Firstly, the corresponding electromagnetic torque and torque ripple of the two motors when the rated current amplitude is 50A are analyzed. As shown in Fig.12(a), the electromagnetic torque of the initial IPM motor is slightly greater than that of the proposed motor, but its torque ripple is obviously greater than that of the proposed motor, so the proposed motor has better stability and is more conducive to the smooth operation of electric vehicles.

Secondly, Fig.12(b) shows the variation of electromagnetic torque performance of two motors with different current angles. Because the motor has a special inductance characteristic of $L_d$>$L_q$, therefore, the proposed motor can obtain positive reluctance torque at a positive *d*-axis current so as to achieve the maximum electromagnetic torque. When the proposed motor operates at a current angle of -5deg, the maximum electromagnetic torque is 86.6Nm, and the *d*-axis current is 4.4A. For the initial IPM motors, the maximum electromagnetic torque is 99.2Nm when the current angle is 35 deg. The *d*-axis current is -28.7A, which is six times of the proposed motor. Such a large negative *d*-axis current also increases the irreversible demagnetization risk of the initial IPM motor, which also verifies that the proposed motor has a lower irreversible demagnetization risk.

### D. Flux-weakening Ability and Speed Range

The proposed motor design in this paper is mainly used in electric vehicles, so the speed range is very important to the motor design. And the biggest advantage of the proposed motor is a wider speed range.

When the motor adopts flux-weakening speed regulation, the

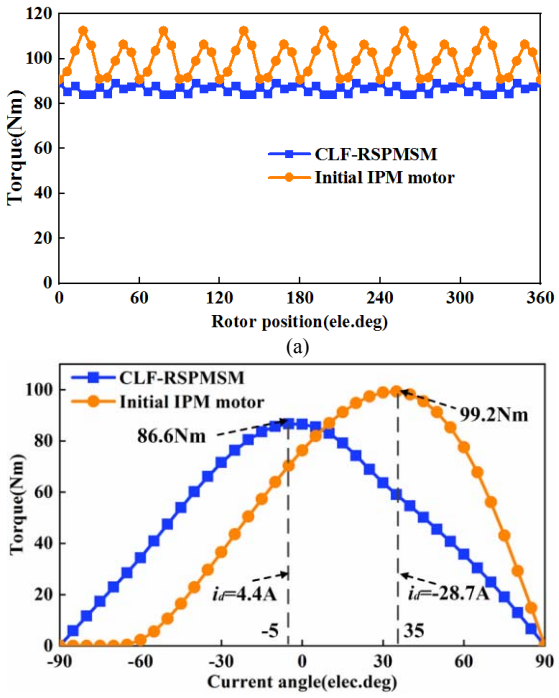


Fig.12. Torque characteristics of the CLF-RSPMSM and initial IPM motor.

speed equation can be derived as follows according to the voltage limit equation:

$$\omega = \frac{U_{lim}}{\sqrt{(\psi_{pm} + L_d i_d)^2 + (L_q i_q)^2}} \tag{12}$$

Where $U_{lim}$ is the limit voltage of the motor. When the voltage of the motor reaches its limit, the PMs chain can be offset by adding an appropriate $d$-axis flux-weakening current. Therefore, when the $d$-axis current is negative, the expression of the motor reaching the ideal maximum speed is as follows:

$$\omega_{max} = \frac{U_{lim}}{\psi_{pm} - L_d i_d} \tag{13}$$

In equation (13), the smaller PM flux linkage and the larger value of $L_d$ are both beneficial to improve the flux-weakening ability and speed range. And the proposed motor has unique inductance characteristics of $L_d$>$L_q$. The larger value of $L_d$ can improve the flux-weakening ability and speed range. And only a small $d$-axis flux-weakening current is needed to reach the same speed range as the initial IPM motor, effectively reducing the irreversible demagnetization risk of the proposed motor. Compared with the RSPMSM, the proposed motor has the characteristics of controllable leakage flux. There is more inter-pole leakage flux, and the PMs flux linkage value decreases during high-speed operation, so the flux-weakening capability of the proposed motor is enhanced. The parameters and operating conditions related to the flux-weakening capacity of the three motors are listed in Table Ⅵ.

Fig.13 shows the torque-speed and power-speed envelops of the two motors. As shown in Fig.13(a), when the rated speed is below, the torque of the initial IPM motor and RSPMSM is slightly higher than that of the proposed motor. However, in the high-speed region, the maximum speed of the initial IPM motor and the RSPMSM are 6600rpm and 8200rpm, respectively, while the maximum speed of the proposed motor can reach

TABLE Ⅵ
FLUX-WEAKENING ABILITY PARAMETERS OF TWO MOTORS

| Items | Initial IPM motor | RSPMSM | CFL-RSPMSM |
|---|---|---|---|
| Rated current(A) | 35 | 35 | 35 |
| Reverse saliency ratio $\varphi_{dq}$ | 0.41 | 1.01 | 1.08 |
| $d$-axis inductance $L_d$(mH) | 7.2 | 9.1 | 9.8 |
| PM flux linkage(Wb) | 0.262 | 0.261 | 0.245 |
| Characteristic current(A) | 36.4 | 28.7 | 25 |

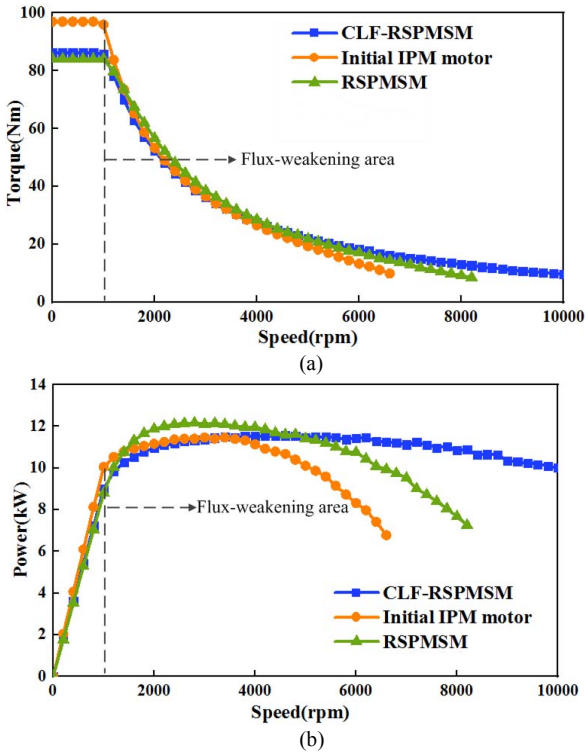


Fig.13. Flux-weakening performance Comparison of the CLF-RSPMSM and initial IPM motor. (a) Torque-speed envelops. (b) Power-speed envelops.

10000rpm. In addition, as shown in Fig.13(b), the constant power speed range of the proposed motor is obviously wider than that of the initial IPM motor and the RSPMSM, so the flux-weakening ability of the proposed motor is better, which is due to the special structure of the rotor of the proposed motor. The rationality of the proposed motor design is verified.

### *E. Efficiency and Loss Comparison*

The motor efficiency Map can well reflect the distribution of motor efficiency under different speeds and torque. In order to facilitate the comparison between the initial IPM motor and the CLF-RSPMSM, the maximum speed is selected as 6000rpm. Fig.14 shows the efficiency map of the two motors. In the high-speed region, the efficiency of the CLF-RSPMSM is significantly higher than that of the initial IPM motor. In addition, the changes of copper and iron loss in the operating area of the two motors are also analyzed. The copper loss Map of the two motors is shown in Fig.15. As the rated current applied by the two motors is the same, there is little difference in copper loss between the two motors in the low speed and high torque operating area. It is worth noting that the difference in iron loss between the two motors is large. Fig.16 shows the iron loss Map of the two motors. When the speed reaches 6000rpm,

the iron loss value of the initial IPM motor is 288W, while the iron loss value of the CLF-RSPMSM is only 46W. This is because there is a large amount of leakage flux in the CLF-RSPMSM under the medium-high speed flux-weakening field state, which can effectively reduce the eddy current loss and hysteresis loss inside the motor. Therefore, the controllable leakage flux characteristics of the CLF-RSPMSM can effectively reduce iron loss in the middle and high speed operating region.

### *F. Demagnetization Risk Comparison*

The irreversible demagnetization of the PMs has a great impact on the performance of the motor, and in severe cases, the motor will be scrapped. In order to discuss the irreversible demagnetization risk of the PMs of the CLF-RSPMSM in operation, the finite-element analysis method was used to study the variation law of the PMs working point of the motor under different magnetization states and the flux density distribution

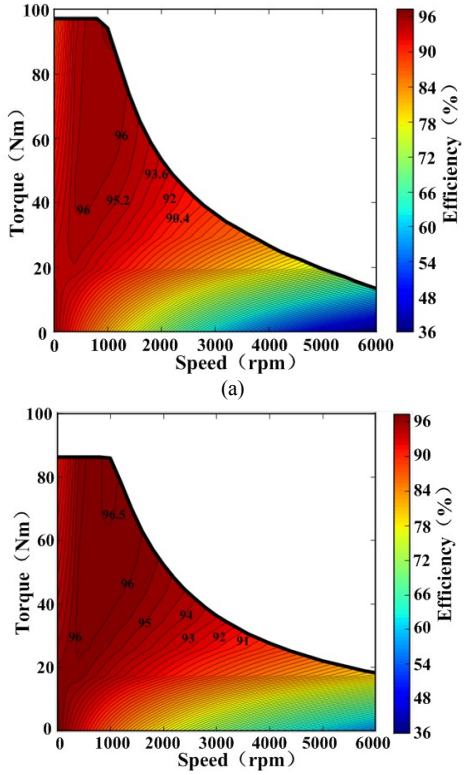


Fig.14. Efficiency Map of the two motors. (a) Initial IPM motor. (b) CLF-RSPMSM.

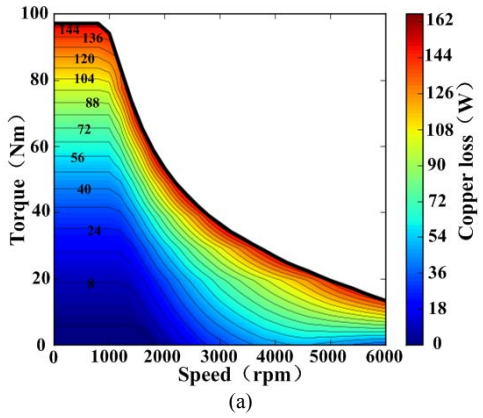


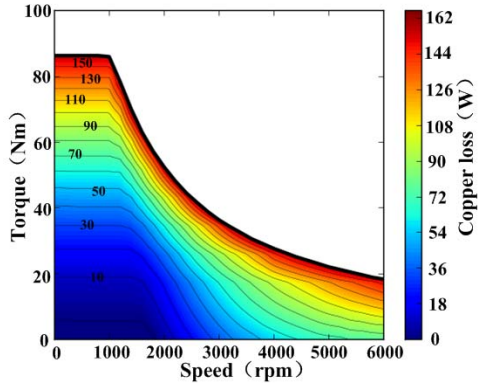


Fig.15. Copper loss Map of the two motors. (a) Initial IPM motor. (b) CLF-RSPMSM.

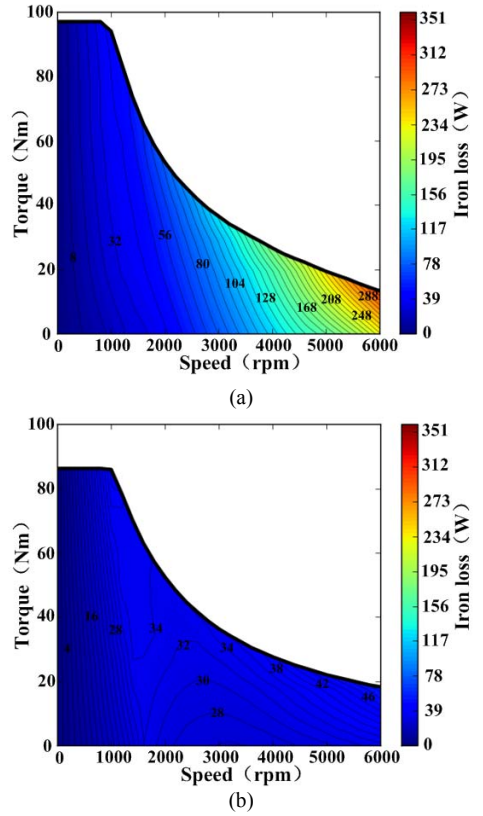


Fig.16. Iron loss Map of the two motors. (a) Initial IPM motor. (b) CLF-RSPMSM.

of the two motors under different operating conditions was compared.

Fig.17(a) shows the flux density distribution of the proposed motor at the rated current. Five observation points are selected on the PMs of the proposed motor. Fig.17(b) shows the variation of the flux density at five observation points under different current angles. It is obvious that the flux density of the five observation points decreases with the increase of the current angle. The maximum flux density occurs at the current angle of -20 deg, which is attributed to the large value of $L_d$ and the characteristic of $L_d$>$L_q$. The magnetic field strength of the PMs can be enhanced by a positive *d*-axis current, thus improving the working point of the PMs. Even in the deep flux-weakening region, the armature current is completely converted into a negative flux-weakening current, and the flux density of

the five observation points is all higher than the limit of demagnetization 0.2T. Therefore, it can be judged that the proposed motor has the excellent capability of resisting irreversible demagnetization risk in the whole operation range. Fig.18 shows the flux density distribution of two motors at different currents. For the convenience of viewing, the selected PM is amplified, and it can be clearly seen that the demagnetization risk of the proposed motor is lower than that of the initial IPM motor. At the same time, point A is selected as the reference point. Fig.19 shows the flux density change curve of working point A at different current. The flux density of the working point of the proposed motor is higher than the initial IPM motor at a different current. Based on the above analysis, the irreversible demagnetization risk of the proposed motor under different working conditions is lower.

## V. STRESS FIELD

In order to make the proposed motor have the characteristics of leakage flux control and Reverse saliency, a reasonable magnetic barrier must be added. This is a test for the mechanical strength of the rotor, so it is necessary to analyze the mechanical stress of the motor at high speed.

The mechanical stress analysis results of RSPMSM and CLF-RSPMSM are shown in Fig.20. The given maximum speed is 10000rpm. Mark the maximum stress position of the two motors as shown in Fig.20(a). The maximum stress of RSPMSM is 121.22MPa, while the CLF-RSPMSM is 84.486MPa. Fig.20(b) shows the stress curve of the two motors with rotation speed. The stress of the RSPMSM at each velocity point is higher than that of the CLF-RSPMSM.

In addition, the deformation distribution of the two motors at a speed of 10000rpm was also analyzed. Fig.21(a) shows the maximum deformation areas of the two motors appeared at the rotor edge. The maximum deformation of the RSPMSM was7.5902 μm, while the maximum deformation of the CLF-RSPMSM was 7.0125μm. Fig.21(b) shows the maximum deformation curve of the two motors with rotation speed. It can be seen that with the increase of speed, the maximum deformation of the CLF-RSPMSM is less than the RSPMSM. Based on the above analysis, the CLF-RSPMSM is more suitable for running at high speed due to its relatively good mechanical strength.

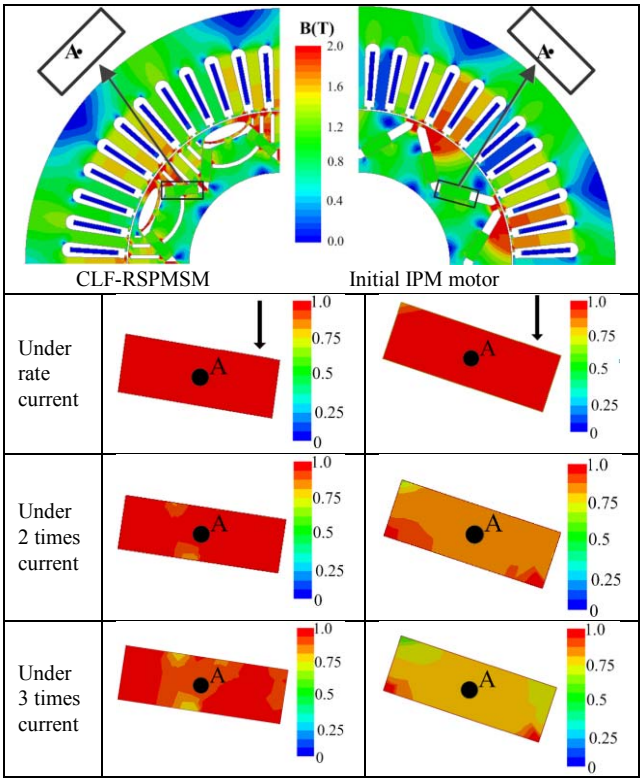


Fig.18. Flux density distribution and of the two motors and PMs under different current.

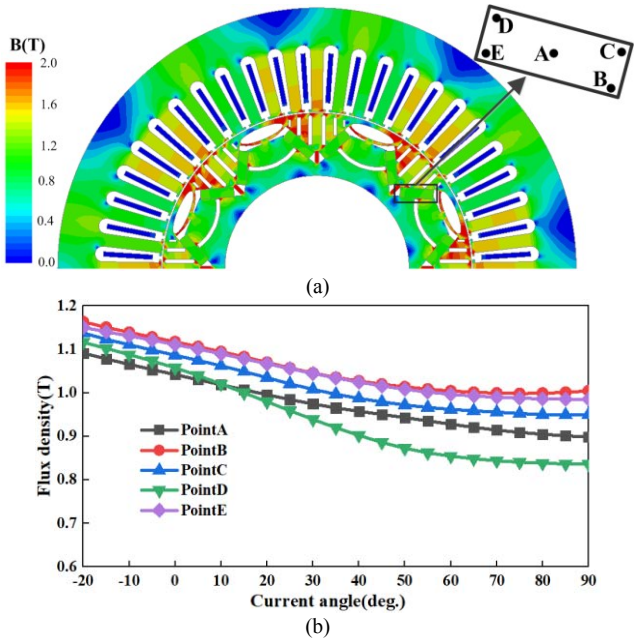


Fig.17. (a) Flux density distribution of the CLF-RSPMSM at rated current condition. (b)Flux density variation with current angle in the CLF-RSPMSM.

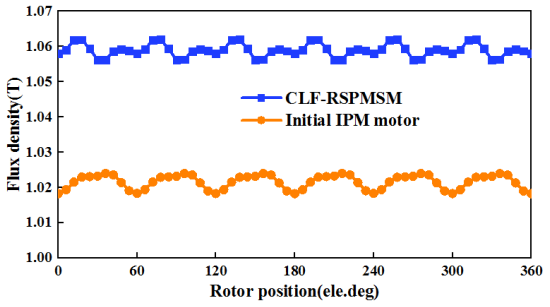


(a) Under rated current($I_{max}$=50A).

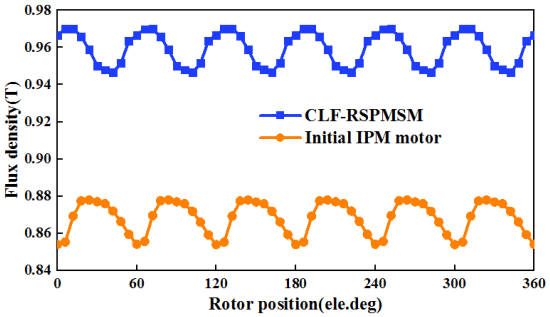


(b) Under 2 times current ($I_{max}$=100A)

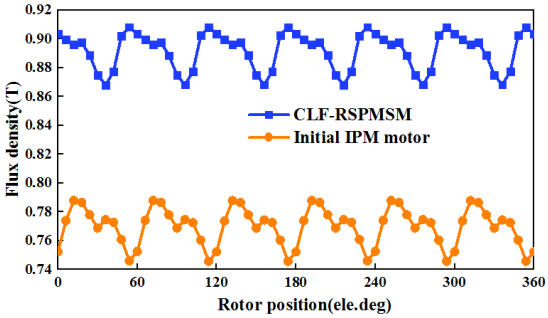


(c) Under 3 times current($I_{max}$=150A).

Fig.19. Changes of the PMs operating point A of the two motors under different currents.

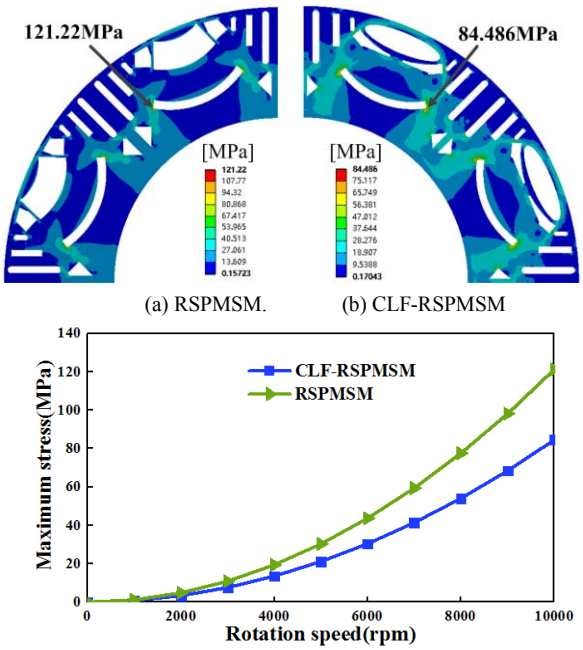


(a) RSPMSM. (b) CLF-RSPMSM

(c) The maximum stress of two motors varies with speed.

Fig.20. Stress analysis of the two motors.

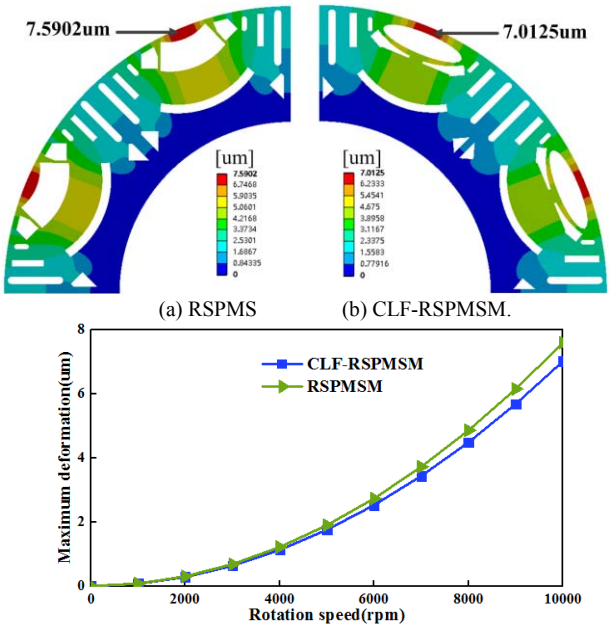


(a) RSPMS (b) CLF-RSPMSM.

(c) The maximum deformation of two motors varies with speed.

Fig.21. Deformation analysis of the two motors.

## VI. Conclusion

In this paper, a controllable leakage flux reverse salient permanent magnet synchronous motor is introduced. By designing the magnetic barrier reasonably, the controllable leakage flux characteristic and the reverse saliency characteristic is realized. Then, a comprehensive sensitivity method and multi-objective optimization method are used to optimize the design objectives of the proposed motor. Finally, the performance of the CLF-RSPMSM and the initial IPM motor are compared and analyzed. The results show that the CLF-RSPMSM has smaller torque ripple, better flux-weakening ability, wider speed range, lower iron loss and stronger resistance to demagnetization. The rationality of the proposed motor design is also verified.

## References

[1] G. Pellegrino, A. Vagati, P. Guglielmi and B. Boazzo, "Performance Comparison Between Surface-Mounted and Interior PM Motor Drives for Electric Vehicle Application," *IEEE Trans. Ind. Electron*., vol. 59, no. 2, pp. 803-811, Feb. 2012.

[2] V. T. Buyukdegirmenci, A. M. Bazzi and P. T. Krein, "Evaluation of Induction and Permanent-Magnet Synchronous Machines Using Drive-Cycle Energy and Loss Minimization in Traction Applications," *IEEE Trans. Ind. Appl.*, vol. 50, no. 1, pp. 395-403, Jan.-Feb. 2014.

[3] X. Liu, H. Chen, J. Zhao and A. Belahcen, "Research on the Performances and Parameters of Interior PMSM Used for Electric Vehicles," *IEEE Trans. Ind. Electron*., vol. 63, no. 6, pp. 3533-3545, June 2016.

[4] X. Zhu, W. Wu, S. Yang, Z. Xiang and L. Quan, "Comparative Design and Analysis of New Type of Flux-Intensifying Interior Permanent Magnet Motors With Different Q-Axis Rotor Flux Barriers," *IEEE Trans. Energy Convers.*, vol. 33, no. 4, pp. 2260-2269, Dec. 2018.

[5] F. Liu, L. Quan, X. Zhu, L. Ge and W. Wu, "Reverse Saliency Optimization of Flux-Intensifying Hybrid Permanent Magnet Machine for Variable Speed Applications," *IEEE Trans. Appl. Supercond.*, vol. 29, no. 2, pp. 1-5, March 2019.

[6] H. Hua and Z. Q. Zhu, "Novel Partitioned Stator Hybrid Excited Switched Flux Machines," *IEEE Trans. Energy Convers.*, vol. 32, no. 2, pp. 495-504, June 2017.

[7] Z. Q. Zhu, Y. S. Chen and D. Howe, "Online optimal flux-weakening control of permanent-magnet brushless AC drives," *IEEE Trans. Ind. Appl.*, vol. 36, no. 6, pp. 1661-1668, Nov.-Dec. 2000.

[8] X. Liu, M. Wang, D. Chen and Q. Xie, "A Variable Flux Axial Field Permanent Magnet Synchronous Machine With a Novel Mechanical Device," *IEEE Trans. Magn.*, vol. 51, no. 11, pp. 1-4, Nov. 2015.

[9] X. Liu, H. Xu, J. Xiao and Y. Zou, "Research on hybrid rotor PMSM with the mechanical flux-adjusting device," in *Proc. of 2019 22nd Int. Conf. on Electrical Machines and Systems (ICEMS)*, Harbin, China, 2019, pp. 1-4.

[10] N. Limsuwan, T. Kato, K. Akatsu and R. D. Lorenz, "Design and Evaluation of a Variable-Flux Flux-Intensifying Interior Permanent-Magnet Machine," *IEEE Trans. Ind. Appl.*, vol. 50, no. 2, pp. 1015-1024, March-April 2014.

[11] T. Kato, M. Minowa, H. Hijikata, K. Akatsu and R. D. Lorenz, "Design Methodology for Variable Leakage Flux IPM for Automobile Traction Drives," *IEEE Trans. Ind. Appl.*, vol. 51, no. 5, pp. 3811-3821, Sept.-Oct. 2015.

[12] A. Athavale, T. Fukushige, T. Kato, C. Yu and R. D. Lorenz, "Variable Leakage Flux IPMSMs for Reduced Losses Over a Driving Cycle While Maintaining Suitable Attributes for High-Frequency Injection-Based Rotor Position Self-Sensing," *IEEE Trans. Ind. Appl.*, vol. 52, no. 1, pp. 234-241, Jan.-Feb. 2016.

[13] X. Zhu, J. Huang, L. Quan, Z. Xiang and B. Shi, "Comprehensive Sensitivity Analysis and Multiobjective Optimization Research of Permanent Magnet Flux-Intensifying Motors," *IEEE Trans. Ind. Electron*., vol. 66, no. 4, pp. 2613-2627, April 2019.

[14] X. Sun, Z. Shi, G. Lei, Y. Guo and J. Zhu, "Multi-Objective Design Optimization of an IPMSM Based on Multilevel Strategy," *IEEE Trans.*

*Ind. Electron*., vol. 68, no. 1, pp. 139-148, Jan. 2021.

[15] X. Zhu, J. Yang, Z. Xiang, M. Jiang, S. Zheng and L. Quan, "Robust-Oriented Optimization Design for Permanent Magnet Motors Considering Parameter Fluctuation," *IEEE Trans. Energy Convers*., vol. 35, no. 4, pp. 2066-2075, Dec. 2020.

[16] X. Zhou, X. Zhu, W. Wu, Z. Xiang, Y. Liu and L. Quan, "Multi-objective Optimization Design of Variable-Saliency-Ratio PM Motor Considering Driving Cycles," *IEEE Trans. Ind. Electron*., vol. 68, no. 8, pp. 6516-6526, Aug. 2021.

**LONGXIN DU** was born in China, in 1997. He received his B.S. degree in Electrical Engineering and Automation from Hunan University of Engineering, Hunan, China, in 2019. He is presently working toward his M.S. degree in Control Engineering at the Jiangxi University of Science and Technology, Ganzhou, China. His current research interests include the design of permanent magnet motors, the controllable leakage flux PMSMs and their multi-objective optimization method.

**XIPING LIU** received his B.S. degree from Hohai University, Nanjing, China, in 1999; his M.S. degree from the Jiangxi University of Science and Technology, Ganzhou, China, in 2004; and his Ph.D. degree in Electrical Engineering from Southeast University, Nanjing, China, in 2009. He is presently working as a Professor in the Department of Electrical Engineering and Automation, Jiangxi University of Science and Technology. His current research interests include the analysis and design of permanent magnet synchronous machine, and wind power technology.

**JIESHENG FU** was born in China, in 1992. He received his B.S. degree in Electrical Engineering and Automation from Jiangxi University of Science and Technology, Jiangxi, Ganzhou, China, in 2016. He is presently working toward his M.S. degree in Control engineering at the Jiangxi University of Science and Technology, Jiangxi, Ganzhou, China. His current research interests include the design and optimization of permanent magnet motor for electric vehicle.

**JIANWEI LIANG** was born in China. He received his B.S. degree from Jiangxi University of Science and Technology, Ganzhou, China; his M.S. degree from the Nanchang University, Nanchang, China. He is presently working as an Associate Professor at the Jiangxi University of Science and Technology. His current research interests include PMSMs, and their drive and control.

**CHAOZHI HUANG** was born in China. He received his B.S. and M.S. degrees in the School of Electrical Engineering and Automation, Jiangxi University of Science and Technology, Ganzhou, China, in 2001 and 2004, respectively. He is presently working towards his Ph.D. degree in the College of Energy and Electrical Engineering, Hohai University, Jiangsu, China. He is presently working as an Associate Professor at the Jiangxi University of Science and Technology. His current research interests include PMSMs and SRMs, and their drive and control, and power electronics applications.